

# Caltech Aerial RGB-Thermal Dataset in the Wild

Connor Lee\*, Matthew Anderson\*, Nikhil Ranganathan, Xingxing Zuo,  
Kevin Do, Georgia Gkioxari, and Soon-Jo Chung

California Institute of Technology

{clee, matta, nrangana, zuox, kdo, georgia, sjchung}@caltech.edu

**Abstract.** We present the first publicly-available RGB-thermal dataset designed for aerial robotics operating in natural environments. Our dataset captures a variety of terrain across the United States, including rivers, lakes, coastlines, deserts, and forests, and consists of synchronized RGB, thermal, global positioning, and inertial data. We provide semantic segmentation annotations for 10 classes commonly encountered in natural settings in order to drive the development of perception algorithms robust to adverse weather and nighttime conditions. Using this dataset, we propose new and challenging benchmarks for thermal and RGB-thermal (RGB-T) semantic segmentation, RGB-T image translation, and motion tracking. We present extensive results using state-of-the-art methods and highlight the challenges posed by temporal and geographical domain shifts in our data. The dataset and accompanying code is available at <https://github.com/aerorobotics/caltech-aerial-rgbt-dataset>.

**Keywords:** Robotics · Semantic segmentation · RGB-T image translation · Visual inertial odometry

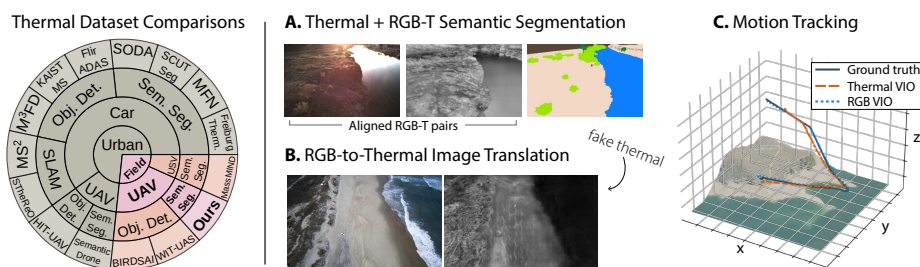


**Fig. 1:** *Left:* Our dataset is uniquely designed to improve thermal scene perception for field robots. *Right:* We provide new benchmarks for thermal-based vision algorithms, including (a) semantic segmentation, (b) image translation, and (c) motion tracking.

## 1 Introduction

Field robots rely predominantly on visual cameras, lidar, and radar to perceive their surroundings [16, 18]. These sensors provide robust perception capabilities,

\* These authors contributed equally to this work.

but falter in low-light and adverse weather conditions [70]. In contrast, thermal cameras use long-wave infrared wavelengths to capture emitted heat, offering dense, visual information in such conditions where other sensors struggle [19]. Recently, they have been used for multimodal perception in autonomous driving and are increasingly being used to enable nighttime robot autonomy [11, 12, 36, 37, 49, 71, 76, 78]. However, successful integration of thermal cameras requires extensive datasets across diverse settings, preventing widespread adoption in field robotics.

Current thermal datasets focus on urban settings for autonomous driving applications (Fig. 1). They comprise of thermal-only imagery [36, 76] or RGB-Thermal (RGB-T) pairs [17, 22, 41, 71], with some including global positioning (GPS/GNSS) and inertial measurements (IMU) for visual-inertial odometry (VIO) and simultaneous localization and mapping (SLAM) [11, 61, 78]. While comprehensive, they lack data depicting natural settings like rivers and forests, which are typical operating areas for field robotics that perform coastline mapping and bathymetry [4] or activity monitoring during forest fires [30].

Due to the lack of thermal benchmarks for algorithms like semantic segmentation and SLAM, field robots cannot easily operate at night or in adverse conditions, requiring online learning [34, 72] or unsupervised domain adaptation to compensate [20, 32, 71], which still require labeled data for evaluation. As such, enabling thermal perception requires collecting and annotating field-specific data from scratch. However, creating a thermal dataset for field robotics is difficult due to two reasons: First, thermal data is hard to crowdsource and web-scrape due to the nicheness of thermal cameras. Hence, acquiring a diverse dataset for algorithm development requires physically going to distinct field locations, increasing time and cost. Second, operating field robots, especially uninhabited aerial vehicles (UAV), usually requires special permits for each location-of-capture.

In this work, we present the first dataset targeting thermal scene perception for field robotics. The dataset consists of oblique-facing imagery captured from a UAV, supplemented with image sets captured at ground level, and focuses on littoral settings within various desert, forest, and coastal environments across the United States. We contribute new benchmarks for thermal and RGB-T semantic segmentation, RGB-T image translation, and VIO/SLAM algorithms, with unique challenges characterized by temporal and geographical domain shifts for learning-based methods and feature sparsity for motion-tracking algorithms. Aside from the proposed benchmarks, our dataset can also be used towards other applications like visual place recognition and terrain-relative navigation.

The paper is organized as follows: Sec. 2 reviews relevant datasets, benchmarks, and algorithms. Sec. 3 describes our dataset details and curation process, and Sec. 4 presents benchmark results. Sec. 5 offers concluding remarks.

## 2 Related Work

### 2.1 Datasets and Benchmarks

**Thermal/RGB-T benchmarks for urban robotics** Current urban thermal and RGB-T datasets primarily focus on autonomous vehicle (AV) technology

**Table 1:** Comparison of datasets captured from aerial platforms. Camera angle of  $90^\circ$  is nadir-pointing. See Tab. S1 in supplement for comparison against thermal datasets captured from surface and ground vehicles.

Dataset	Task	RGB	Thermal	GPS	IMU	Setting	Location	# Samples	Camera pose
ViaDrone [83]	Obj. Det.	✓	✗	✗	✗	Urban	China	10,209	Variable
HIT-UAV [67], NH-CU [63]	Obj. Det.	✓	✓	✗	✗	Urban	China, Japan	2,898 - 5,880	$30^\circ$ - $90^\circ$ , 60-130 m
WIT-UAS [30]	Obj. Det.	✗	✓	✓	✓	Forest	USA	6,951	$30^\circ$ , $90^\circ$ , < 120 m
BIRDSEI [3]	Obj. Track.	✗	✓	✗	✗	Savannas	S. Africa	62,000	Off-nadir, 60-120 m
AeroScapes [48], UAVid [45], [10], [6], Swiss/Okutama [63]	Sem. Seg.	✓	✗	✗	✗	Urban	China, Japan, Switzerland	191 - 3269	$30^\circ$ - $90^\circ$ , < 100 m
Semantic Drone Dataset [47]	Sem. Seg.	✓	✓	✗	✓	Urban	Germany	400	$90^\circ$ , < 30m
<b>Ours</b>	Sem. Seg.	✓	✓	✓	✓	River, Coast, Lake, Mountain, Desert	USA	4,195	$20^\circ$ , $45^\circ$ , < 120 m

and surveillance applications. AV-related datasets cover tasks such as object detection [11, 17, 41], semantic segmentation [22, 36, 71, 76], and localization [11, 61, 78]. Some include data from other spectra, benchmarking not only thermal algorithms but also RGB-T [11, 22, 41, 63, 71] and other multispectral models. In contrast, datasets for surveillance applications use fixed cameras [29] and UAVs [63, 67] to detect personnel, vehicles, and other objects. Despite many urban thermal benchmarks, they cannot be directly used to develop algorithms for robots operating in natural environments due to the domain gap.

**Thermal/RGB-T benchmarks for field robotics** Datasets for robots operating in non-urban environments remain limited. MassMIND [49] and PST900 [62] benchmark thermal semantic segmentation for maritime and subterranean robotic environments, respectively. WIT-UAS [30] provides UAV-borne thermal images for object detection in wildfire-prone environments. One work [34] proposes an aerial RGB-T dataset for thermal water segmentation in littoral areas but only provides 1272 labels consisting of a single *water* class. Benchmarks like [3, 7] depict natural environments but are targeted towards wildlife tracking. To address this gap, we present an aerial RGB-T dataset which can be used to benchmark multiple tasks, including semantic segmentation, RGB-T image translation, and localization, across diverse natural environment robotic applications. Specifically, we build upon the dataset from [34] by extending the number of semantic classes from 1 to 10 and adding additional RGB-T data captured from air and ground, resulting in a total of 4195 semantic segmentation annotations. In comparison to existing thermal/RGB-T datasets, our dataset can enable nighttime field robotic applications like remote sensing research, geological sampling, precision agriculture, and wilderness search and rescue.

**UAV-based semantic segmentation datasets** Aside from [34], existing UAV-captured semantic segmentation datasets [6, 10, 45, 47, 48, 63] cover urban environments (Tab. 1). With the exception of [47] which provides 400 thermal image samples, all of these datasets contain only RGB data for semantic segmentation. While they provide images with relevant view angles, the modality gap and focus on urban content makes them impractical for aerial field robotic applications.

## 2.2 Algorithms using Thermal Datasets

**Thermal semantic segmentation** Since thermal images are spatially identical to their RGB counterparts, popular RGB semantic segmentation algo-

rithms [5, 8, 53, 74] can be applied directly. However, some works [36, 51, 76] develop models specifically for thermal imagery, and leverage edge priors to overcome low resolution and blurriness due to thermal crossover [56]. Although specifically designed for thermal, these models only marginally outperform standard RGB segmentation models [51] and their performance in field settings, where edges are less structured, remains untested. Aside from architectural advancements, improvements in thermal semantic segmentation come from domain adaptation (DA) methods [20, 36, 69, 71] that use labeled RGB data with unlabeled thermal data. To provide fair comparisons, we do not provide DA baselines in our benchmarks as performance varies based on the choice of RGB data.

**RGB-T semantic segmentation** RGB-T semantic segmentation methods compensate for the weaknesses of each modality via deep feature fusion, data augmentation, and adversarial training. Most approaches [22, 60, 65, 66, 79] utilize encoder-decoder architectures with modality-specific encoders and shared decoders, and show significant improvements over channel-stacked RGB-T inputs. Works like [39, 81] make improvements by integrating RGB and thermal features at multiple stages within the encoders, while [62] eschews RGB-T training pairs by processing RGB-T inputs sequentially. Other methods include random input masking to reduce reliance on a single modality [60] and adversarial training to adapt to different times of day [71].

**RGB-T image translation** RGB-T image translation is vital as it may enable thermal training data to be generated from large-scale RGB datasets. Works based on generative adversarial networks (GAN) such as [27, 35, 42, 52, 82] can be used without RGB-T image pairs. However, GANs like [28, 73] that require paired imagery provide better translations for both visual appeal and domain adaptation [36]. Recent diffusion methods [57, 58] have demonstrated remarkable results on RGB imagery, but have not been tested on RGB-T image translation.

**Thermal VIO and SLAM** Low signal-to-noise ratio, reduced contrast, and blurred boundaries in thermal images present challenges for VIO and SLAM. Several studies [2, 13, 14, 24, 26] use indirect methods by tracking keypoints extracted from thermal images for visual constraints and rely on image normalization techniques to improve keypoint extraction. In contrast, [31] uses a direct method to extract and track high-gradient points by minimizing radiometric error. Other works utilize learned local and global features to improve feature tracking [80] and loop closure detection [59], respectively.

### 3 The Caltech Aerial RGB-Thermal Dataset

#### 3.1 Data Acquisition Hardware

To capture this dataset, we developed a custom sensor stack with synchronized RGB-thermal imagery, IMU, and global positioning data (Fig. 2). The sensor stack features a non-radiometric FLIR ADK thermal camera (640×512 px and 75° horizontal FoV, 60 Hz) flanked by a pair of FLIR Blackfly electro-optical (EO) monochrome and color cameras<sup>1</sup> (960×600 px and 75° horizontal FoV, 30 Hz).

<sup>1</sup> BFLY-U3-23S6M-C mono/color with Tamron M112FM08 lenses



Pose information is provided by a VectorNav VN100 IMU (200 Hz) and a u-blox M8N GPS (5 Hz). All three cameras and the VN100 are hardware synchronized using a dedicated signal generator and are rigidly attached to each other using a stiff, 3D printed mount. A Simply NUC Ruby Mini PC (AMD Ryzen 7 4800U, 32 GB RAM) is used for the compute, and the entire system is interfaced using ROS Noetic. Our cameras and IMU were calibrated following the procedures found in Supplementary Material Sec. S2.2 and were not disassembled from each other between any of the dataset collections.

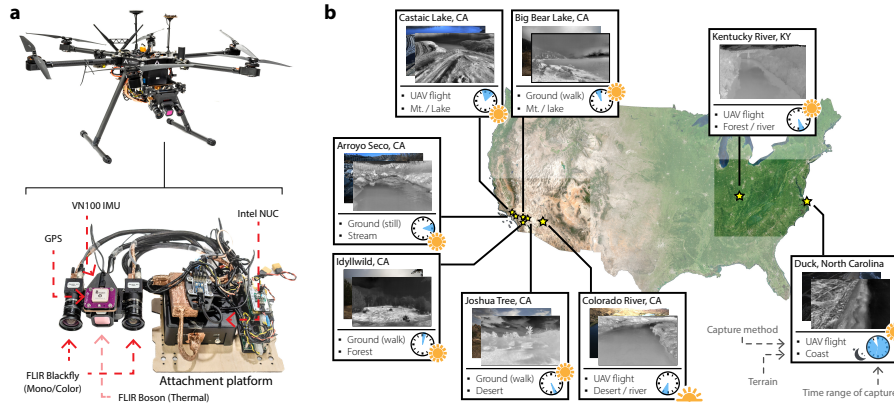


**Fig. 2:** (a) The Aurelia X6 hexacopter and sensor stack used to capture our aerial dataset. (b) Geographic distribution of our data collection sites and collection times.

The sensor stack is mounted rigidly onboard an Aurelia X6 hexacopter (Fig. 2) without gimbal stabilization at angles between  $0^\circ$  (level with the horizon) to  $45^\circ$  downwards to provide different viewpoints. When mounted to a UAV, we also log the position and attitude estimates from the UAV at 20 Hz providing improved positioning accuracy from the onboard RTK GPS. Additionally, the sensor stack’s modularity allows us to capture datasets on foot by mounting it to a tripod where flight restrictions are in-place.

### 3.2 Data Collection and Processing

**Data capture** We captured 37 aerial and ground trajectories covering lakes, rivers, coastlines, deserts, and mountains from around Southern California, Kentucky, and North Carolina (Fig. 2). Aerial trajectories (18) involve high motion with intermittent hovering, and mostly depict scenes from 40 m altitude. Ground-level trajectories (19) were captured on foot, with 7 captured without any movement for VIO debugging purposes. For more details, see Supplementary Materials Tab. S2 and Sec. S2.1.

**Thermal image normalization** For the baselines presented in this work, we typically normalize 16-bit thermal data by rescaling between the 1<sup>st</sup> and 99<sup>th</sup> percentile pixel values and follow with contrast limited adaptive histogram equalization (CLAHE). We keep normalized data as floats to minimize information loss, and only convert to 8-bit format when necessary or for visualization.

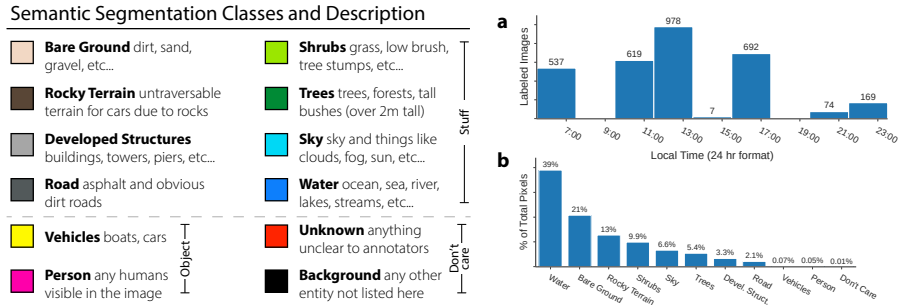


**Fig. 3:** Semantic segmentation classes in our dataset. The color mapping is used throughout this paper. (a) Hourly distribution of annotated thermal images. (b) Histogram of semantic classes.

**Semantic segmentation annotation** To aid development of scene perception algorithms for field robots, we manually-annotated a subset of thermal images for semantic segmentation with classes in Fig. 3. To avoid redundancy, images were sampled every 3s when moving and every 20s when still, resulting in 4195 samples. We considered a frame in motion if the distance moved within the past 2 seconds exceeded 0.5 meters, with distances computed using GPS coordinates.

To promote labeling consistency, annotators pre-read descriptions of each trajectory, which contained a list of classes present, labeled examples provided by the authors, and GPS coordinates (for Google Earth look-up). Annotators were then given an RGB-T image pair with trajectory metadata and asked to label the thermal frame. Annotations were reviewed by authors, with inconsistent or incorrect labels sent back. 3 rounds of annotation were done, with the final and initial set of labels differing by 0.08 mIoU. Classes most frequently re-annotated were *bare ground*, *rocky terrain*, *road*, *trees*, and *vehicles*.

**RGB-thermal image alignment** To align thermal and RGB image pairs, we stereo rectified the RGB-T image pairs using the camera matrices obtained from calibration (Sec. S2.2) and projected the thermal image into the larger RGB image frame to preserve RGB resolution. As our baseline is small compared to the depth of the scenes we capture, image pairs are near-coregistered after rectification. Due to differences in optics, the field-of-view of the aligned image pairs is narrower compared to that of the thermal camera.

### 3.3 Dataset Splits

**General (benchmark) split** This is our primary split for semantic segmentation and image translation benchmarks. We randomly partition the annotated thermal dataset (Sec. 3.2) into train/val/test sets at a 75:12.5:12.5 ratio.

**Temporal split** To promote studies into the effect of different time-of-day capture of the thermal images, we split the dataset using three time periods: twilight/sunrise (5 AM - 7 AM), daytime (10 AM - 5 PM), and nighttime (7 PM - 4 AM). We randomly partition the daytime images into train/val/test sets using the ratio from above and leave the twilight and nighttime sets for testing.

**Geographical split** The geographical splits are intended to test algorithm adaptability to unseen settings. We provide two splits:

1. *Terrain-based*: This split partitions data into the following terrain categories: aerial river, aerial lake, aerial coast, and ground-captured images. Train/val/test splits are created per category with a 50:15:35 ratio.
2. *Region-based*: This is based on the area of the United States where the data was captured. Distinct regions include California (CA), Kentucky (KY), and North Carolina (NC), with train/val/test created in the same way as above.

## 4 Experiments

We provide baselines for the following benchmarks: thermal semantic segmentation, RGB-T semantic segmentation, RGB-T image translation, and VIO/SLAM. Furthermore, we explore the zero-shot thermal segmentation capabilities of large vision-language models on our dataset and perform further ablation studies.

**Table 2:** Supervised model performance (mIoU), framerate (FPS at batch size 1), and floating point operations (FLOP) for various semantic segmentation network baselines.

Model	Bare ground	Rocky terrain	Develop. struct.	Road	Shrubs	Trees	Sky	Water	Vehicles	Person	Stuff	Object	All	Orin (GPU)	NUC (CPU)	FLOPS (G)
FastSCNN [53]	0.807	0.907	0.728	0.631	0.694	0.776	0.956	0.965	0.384	0.058	0.808	0.221	0.690	<b>124.2</b>	<b>85.6</b>	<b>1.0</b>
MobileNetV3-S 0.75 [25]	0.802	0.914	0.676	0.633	0.704	0.814	0.955	0.976	0.383	0.111	0.809	0.247	0.697	75.2	24.0	3.3
MobileNetV3-L 0.75	0.801	0.914	0.701	0.615	0.713	0.793	0.959	<b>0.976</b>	0.432	0.148	0.809	0.290	0.705	59.0	15.5	4.8
MobileViT-V2 0.50 [46]	0.822	0.913	0.759	0.650	0.694	0.781	0.954	0.970	0.222	0.030	0.818	0.126	0.680	60.1	10.7	5.5
EfficientViT-B0 [5]	0.825	0.917	<b>0.777</b>	0.618	0.710	0.793	0.961	0.965	0.495	<b>0.191</b>	0.821	<b>0.343</b>	<b>0.725</b>	51.2	5.5	3.9
EfficientNet-Lite0 [68]	0.819	0.908	0.769	0.601	0.709	0.805	0.962	0.968	0.380	0.079	0.818	0.229	0.700	47.7	12.8	7.2
EfficientNet-Lite2	<b>0.825</b>	0.920	0.765	0.614	0.698	0.805	0.958	0.971	0.386	0.118	0.820	0.252	0.706	38.9	11.2	9.4
Segformer-B0 [74]	0.804	0.910	0.690	0.624	0.696	0.788	0.960	0.970	0.195	0.000	0.805	0.097	0.664	38.3	5.9	10.2
Segformer-B1	0.814	0.909	0.773	0.603	0.713	0.799	0.960	0.965	0.366	0.000	0.817	0.183	0.690	30.3	3.5	19.9
ResNet18 [23]	0.810	0.905	0.766	0.618	0.711	0.807	0.959	0.966	0.431	0.158	0.818	0.294	0.713	69.3	12.4	22.4
ResNet50	0.819	0.916	0.747	<b>0.658</b>	0.711	0.799	0.961	0.974	0.361	0.182	0.823	0.272	0.713	29.9	6.1	45.4
ResNeXt50 [75]	0.825	0.919	0.773	0.653	0.709	0.794	0.964	0.976	0.436	0.137	<b>0.827</b>	0.287	0.719	23.0	5.6	45.5
ConvNext-T [44]	0.799	0.909	0.719	0.608	0.706	0.808	0.961	0.970	0.363	0.003	0.810	0.183	0.685	25.8	3.3	47.4
ConvNext-S	0.810	0.913	0.771	0.603	<b>0.718</b>	0.810	0.965	0.964	0.492	0.048	0.819	0.270	0.709	19.1	2.3	75.0
ConvNext-B	0.810	<b>0.921</b>	0.697	0.611	0.706	0.803	0.963	0.972	0.348	0.112	0.811	0.230	0.694	14.6	1.4	130.5
ConvNext-B (CLIP) [55]	0.813	0.918	0.683	0.632	0.718	0.813	<b>0.965</b>	0.972	<b>0.517</b>	0.137	0.814	0.327	0.717	14.6	1.4	130.4
ConvNext-B (CLIP) ✳	0.773	0.887	0.713	0.487	0.656	0.756	0.946	0.951	0.158	0.019	0.771	0.089	0.635	14.6	1.4	130.4
DINOv2 [50] (linear head)	0.800	0.907	0.681	0.606	0.693	0.796	0.956	0.967	0.375	0.079	0.801	0.227	0.686	15.2	2.1	—
DINOv2 (linear head) ✳	0.705	0.844	0.619	0.419	0.558	0.725	0.922	0.920	0.356	0.158	0.714	0.257	0.623	15.2	2.1	—
DINOv2 (nonlin. head)	0.810	0.916	0.708	0.635	0.700	<b>0.819</b>	0.959	0.973	0.399	0.119	0.815	0.259	0.704	15.2	2.1	—
DINOv2 (nonlin. head) ✳	0.796	0.903	0.732	0.606	0.691	0.794	0.954	0.963	0.471	0.149	0.805	0.310	0.706	15.2	2.1	—
FTNet <sup>†</sup> [51]	0.755	0.867	0.635	0.576	0.643	0.653	0.787	0.947	0.234	0.024	0.733	0.129	0.613	11.1	1.4	100.5

<sup>†</sup>Thermal-specific model ✳ Frozen encoder

### 4.1 Thermal Semantic Segmentation

We run multiple baselines on our general split before choosing a specific model to test on the geographic and temporal splits. We go over our baselines before analyzing their performance on our benchmarks.

**Baselines** Motivated by robotic applications, we are interested in both inference speed and segmentation performance. Our baselines place an emphasis on lightweight, real-time networks, but also on foundation models like DINOv2 [50] and ConvNext-B (CLIP) [44, 55] to explore any latent multimodal capabilities. We also test a thermal-specific model, FTNet [51], which uses an edge-based loss function to compensate for blurred boundaries in thermal images.

Besides FastSCNN [53], EfficientViT [5], Segformer [74], DINOv2, and FTNet, all network encoders in Tab. 2 feed into a DeepLabV3+ segmentation head. In particular, DINOv2 was employed with linear and non-linear, multi-scale

heads in order to study the generalization capacity of its pretrained features to the thermal modality. All baselines except DINOv2 and ConvNext-B (CLIP) were trained from pretrained ImageNet weights. All networks, besides FTNet, were trained using the cross entropy loss. Further details on baseline implementation and training can be found in Supplementary Material Sec. S3.1.

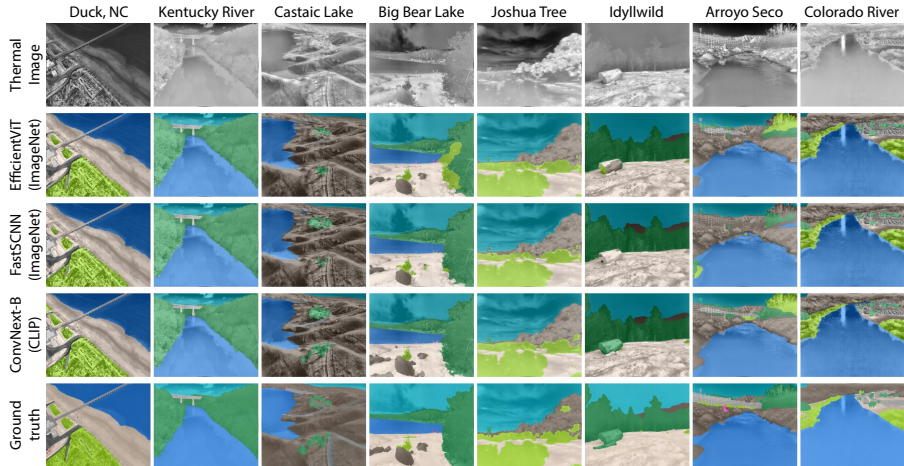


**Fig. 4:** Thermal images and semantic segmentation labels from each capture area with inference results from EfficientViT, FastSCNN, and ConvNext-B (CLIP).

**General benchmark** We use the general (random) split (Sec. 3.3) to compare thermal semantic segmentation performance between baselines (Tab. 2). With field robotic applications in mind, we analyze segmentation results in context of GPU and CPU frame rates, which were measured onboard the Nvidia Jetson AGX Orin (GPU) and the Ruby NUC (CPU) embedded platforms, respectively<sup>2</sup>.

In general, we found that larger models provide marginal benefit over smaller, compute-efficient models. In particular, a 0.027 mIoU difference between the largest (ConvNext-B) and fastest (FastSCNN) baselines comes at the cost of  $130\times$  more FLOPs. Overall, EfficientViT-B0 performed the best, attaining the highest mIoU (0.725) while performing 50 Hz inference on the Jetson AGX Orin.

While large RGB foundation models show little gain over ImageNet pretraining, their features do extend to the thermal modality. Specifically, a frozen DINOv2 (linear head) outperforms the thermal-specific FT-Net. With a nonlinear head, it matches the performance of other end-to-end trained networks. While this shows the benefit of large-scale RGB pretraining, the choice of RGB pretraining data or learning strategy seems to matter. Notably, the frozen ConvNext-B (CLIP) model gives marginal gain over the frozen DINOv2 (linear head), despite a larger, nonlinear segmentation head. Overall, foundation models do not confer

<sup>2</sup> Models of input size  $512\times 640$  were converted to ONNX and inference speed was averaged over 50 forward passes after a warm-up period.

significant performance advantages for semantic segmentation on our dataset in order to justify their computational cost.

Overall, all baselines can segment *stuff* classes well but none excel with the rare *object* classes: *vehicle* and *person*. Future models would likely need to consider weighted loss functions, smarter data augmentation, or domain adaptation techniques in order to improve on object classes. Lastly, we note that the thermal-specific model, FTNet, performs poorly, likely as its edge priors are less effective in unstructured, natural environments compared to urban environments.

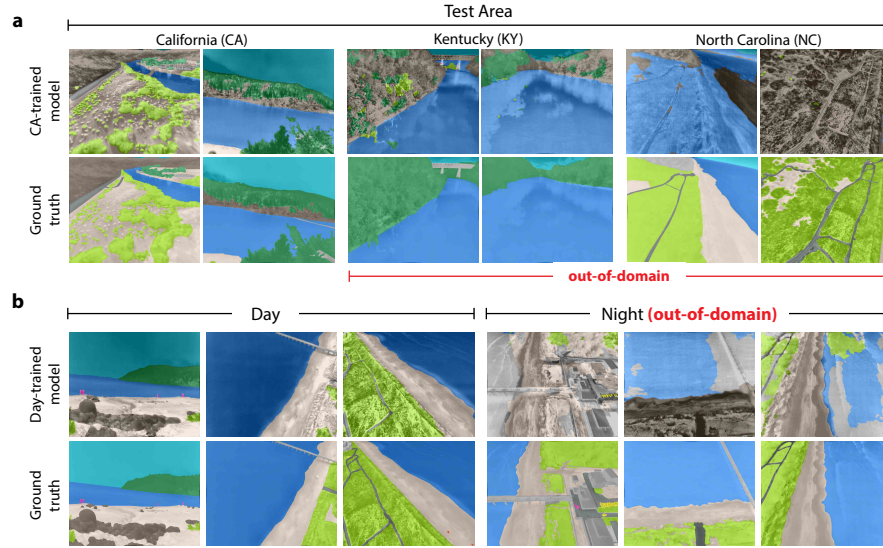


**Fig. 5:** (a) Thermal semantic segmentation failures due to intra-class semantic variations when testing on geographically-partitioned, *out-of-domain* data. (b) Failures due to photometric variations between day (*in-domain*) and night (*out-of-domain*).

**Geographically-partitioned benchmarks** We retrained our best baseline (Tab. 2) on geographically-partitioned sets to evaluate intra-thermal generalization. Given the cost and effort of collecting diverse aerial thermal data of field settings, we aim to determine the minimum amount of annotated data required to effectively deploy. Using EfficientViT-B0, we performed two experiments to study generalization across difference geographic regions and terrain types.

**Table 3:** Thermal semantic segmentation results on geographically-split data

(a) Region-based split					(b) Terrain-based split				
Train Area	Test Area			Avg. mIoU	Training Terrain	Testing Terrain			Avg. mIoU
	CA	NC	KY			River	Lake	Coast	
CA	0.666	0.084	0.193	0.314	River	0.668	0.196	0.117	0.327
NC	0.084	0.508	0.031	0.208	Lake	0.196	0.364	0.061	0.207
All	0.648	0.525	0.587	0.586	Coast	0.127	0.119	0.522	0.256
					All	0.646	0.415	0.493	0.518
					All + ground	0.658	0.416	0.520	0.532

In the first experiment, we trained on thermal data from CA and tested on images from KY and NC (Tab. 3a). Despite common classes in each region, results show poor generalization to class variations across geographic areas. We see this again when repeating with the NC split. In the second experiment, we divided our data into three terrain types, *aerial river*, *aerial lake*, and *aerial coast*. Remaining ground-captured images were lumped into a fourth *ground* category. We trained and tested all pairwise combinations and found poor generalization across terrain types as well (Tab. 3b). Notably, we found low, in-domain performance for the lake setting but saw gains after training on aerial data from other terrain and further improvements after training on ground level images. Overall, our results reiterate the benefit of having training data representative of the testing environment, but also show that gains can be made by including out-of-domain (OOD) data from different terrain and different viewpoints.

Overall, the geographic benchmark presents a difficult domain adaptation problem, requiring both inter- and intra-modality domain adaptation techniques to overcome. Although such techniques could perform well in this challenge, the results also highlight a need for an even larger and more diverse thermal dataset capturing common field environments than what we presented.

**Temporally-partitioned benchmark** Here, we assess EfficientViT-B0’s performance against intra-thermal, temporal distribution shift due to thermal inversion. We train the model on images from the daytime and test on images captured at sunrise and at night. The model achieved mIoUs of 0.242 at sunrise, 0.193 at night, and 0.777 on a separate daytime test split. Despite training on daytime images from the same location, the model fails on nighttime scenes, struggling to classify *water* due to thermal inversion (Fig. 5b). As such, to perform well on this split, future algorithms need to augment datasets to simulate such inversions or intentional collect data capturing such phenomena.

**Table 4:** RGB-Thermal semantic segmentation network baseline results (mIoU).

Model	Bare ground	Rocky terrain	Devel. struct.	Road	Shrubs	Trees	Sky	Water	Vehicles	Person	All	FLOPS (G)
RGB Only <sup>†</sup>	0.790	0.873	0.808	0.559	0.664	0.752	0.891	0.967	0.399	0.000	0.670	45
Thermal Only <sup>†</sup>	0.766	0.835	0.789	0.536	0.654	0.749	0.907	0.971	0.399	0.000	0.661	45
EAEFNet [39]	0.805	0.863	0.813	0.545	0.702	0.802	<b>0.937</b>	0.976	0.481	0.000	0.692	358
CRM [60]	0.816	<b>0.900</b>	0.851	<b>0.616</b>	0.695	0.779	0.923	0.974	0.377	<b>0.206</b>	0.714	310
CMNeXt [79]	<b>0.830</b>	<b>0.900</b>	<b>0.861</b>	0.607	<b>0.718</b>	<b>0.808</b>	0.933	<b>0.980</b>	<b>0.560</b>	0.190	<b>0.740</b>	148

<sup>†</sup> DeepLabV3+ (w/ ResNet50 encoder)

## 4.2 RGB-T Semantic Segmentation

We use the paired RGB-T dataset (Sec. 3.2) and partition it using the general split (Sec. 4.1). Recall that RGB and thermal input sizes are  $960 \times 600$  pixels and the thermal FoV is narrower than in the previous benchmarks (Sec. 4.1).

**Baselines** We test three RGB-T semantic segmentation algorithms achieving state-of-the-art results in urban RGB-T scene segmentation benchmarks: CRM [60], EAEFNet [39], and CMNeXt [79]. To compare against single-modality mod-



**Table 5:** RGB-Thermal image translation results

Method	Method Type	RGB $\rightarrow$ Thermal		
		PSNR $\uparrow$	SSIM $\uparrow$	mIoU $\uparrow$
UNIT [42]	Unpaired GAN	12.85	0.421	0.189
MUNIT [27]	Unpaired GAN	16.08	0.459	0.173
Edge-guided RGB-T [35]	Unpaired GAN	12.20	0.436	0.225
Pix2Pix [28]	Paired GAN	<b>20.06</b>	0.547	0.354
Pix2PixHD [73]	Paired GAN	20.05	<b>0.579</b>	0.379
VQGAN [15]	Paired GAN	18.09	0.540	<b>0.388</b>
Palette [58]	Paired Diffusion	11.51	0.399	0.194

els, we train two additional ResNet50/DeepLabV3+ segmentation models on RGB and thermal data accordingly (Sec. 4.1).

**Performance analysis** All RGB-T models outperform the single-modality baselines, with CMNeXt outperforming the next best RGB-T model by 0.026 mIoU (Tab. 4). Overall, incorporating RGB imagery into the segmentation pipeline greatly improved the distinction between land-based *stuff* classes which can be hard to distinguish in thermal due to thermal crossover. However, these improvements come at a high computational cost and would not be suitable for field robotic applications. Excelling in this benchmark would involve improving the segmentation performance of the *object* classes, possibly by leveraging RGB data in unsupervised domain adaptation training schemes.

### 4.3 RGB-Thermal Image Translation

We use the RGB-T paired dataset from Sec. 4.2 to benchmark image translation algorithms operating in the RGB $\rightarrow$ T direction.

**Baselines** We benchmark GAN methods that need RGB-T pairs (Pix2Pix [28], Pix2PixHD [73], VQGAN [15]) and unpaired methods (UNIT [42], MUNIT [27], [35]) that do not. We also evaluate Palette [58], a paired diffusion approach.

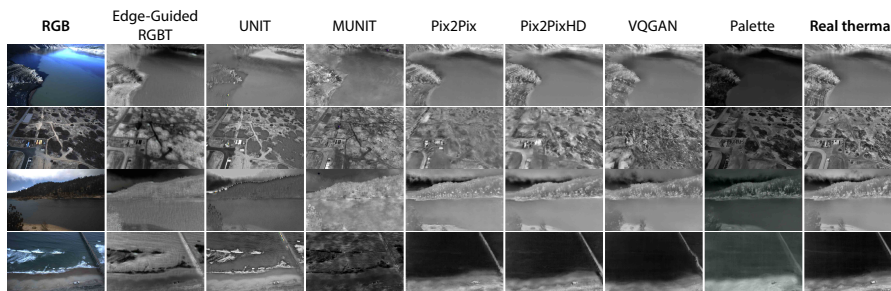


**Fig. 6:** RGB-to-thermal image translation results. Zoom-in to see fine-details.

**Image translation metrics** We quantify RGB-T image translation using the Peak-Signal-to-Noise ratio (PSNR) and the Structural Similarity Index (SSIM). In addition, we propose a third metric: the thermal mIoU. This is equivalent to the FCN-score used in RGB image translation works [28]. Instead of an RGB network, our metric uses our EfficientViT thermal segmentation network (Tab. 2) to segment translated thermal images before evaluating with ground truth.

**Performance analysis** Paired GANs outperform unpaired GANs and diffusion methods, achieving higher values across all three metrics (Tab. 5). Qualitative assessment (Fig. 6) shows poor translations from unpaired techniques, with most retaining geometric artifacts unique to RGB (ocean waves and shadows) and ignoring relative temperature characteristics. Paired GANs produce results similar to real thermal images but with inconsistent details upon closer inspection. Likewise, the diffusion method produces accurate translations but is not consistent. Overall, RGB-T translation still requires improvements before being able to provide a reliable source of thermal training data from existing RGB datasets. For domain adaptation purposes, we emphasize that maximizing the thermal mIoU score is more important than photometric consistency.

#### 4.4 Motion Tracking

To quantify VIO/SLAM robustness, we select 12 clipped sequences from our dataset ranging in motion tracking difficulty: from urban sports fields (easy) to our natural environments (hard). We normalize thermal images using the 5<sup>th</sup> and 95<sup>th</sup> percentile pixel values (Sec. 3.2) to enable feature detection.

**Table 6: VIO/SLAM performance (Absolute Trajectory Error [m]) on aerial sequences**

Method	Type	Modality	North Field						Castaic Lake, CA				Duck, NC	
			N1	N2	N3	N4	N5	N6	C1	C2	C3	C4	D1	D2
VINS-Fusion	SLAM	RGB	2.883	7.530	4.036	2.009	4.045	0.834	1.555	—	3.277	1.566	1.031	0.700
VINS-Fusion		Thermal	9.454	12.26	9.854	2.926	11.00	5.114	7.296	1.513	5.321	2.025	0.879	—
VINS-Fusion	VIO	RGB	5.458	9.509	6.518	2.121	6.026	1.277	1.555	—	3.277	1.377	1.031	0.725
VINS-Fusion		Thermal	13.82	12.86	11.99	2.926	13.98	5.194	7.284	10.60	5.321	2.034	0.879	—
Open-VINS	VIO	RGB	22.80	36.15	37.15	5.165	—	3.896	—	3.573	—	—	0.475	0.700
Open-VINS		Thermal	14.43	30.64	16.12	2.258	—	1.562	—	5.311	—	—	1.073	—
Trajectory length (m)			1533	1326	1253	153	1104	642	310	65	174	137	88	80

**Baselines** We evaluate VINS-Fusion [54] (graph optimization-based) and Open-VINS [21] (filtering-based). We test VINS-Fusion in VIO and SLAM modes, with and without loop closure constraints, respectively, and report Absolute Trajectory Error [64] averaged over four runs.

**Performance analysis** This benchmark reveals challenges due to fast motion at altitude and periodic feature sparsity in littoral environments. In such scenes, motion tracking frequently failed due to loss of features, requiring sequences to be clipped for quantifiable evaluations (Tab. 6). VINS-Fusion outperformed Open-VINS mainly due to higher feature tracking reliability. VINS-Fusion works better on RGB images than on thermal images in general. However, VINS-Fusion demonstrates superior feature tracking on thermal images compared to RGB on the C2 sequence of Castaic Lake, where the thermal contrast of stone grains on the lake coast was particularly pronounced in the late afternoon. This observation motivates future research on integrating thermal and RGB cameras for motion tracking with enhanced robustness and versatility. Our benchmark presents a difficult challenge for VIO and SLAM algorithms in extreme environments where water and reflections off water surfaces dominate image scenes, providing a unique test bed to invigorate interest in robust feature matching and motion tracking in natural texture-deficient scenarios.



**Table 7:** RGB foundation model performances on thermal imagery

(a) Instance segmentation via SAM on thermal and augmented color images using coregistered color image segmentations as ground truth (b) Zero-shot semantic segmentation (mIoU) on coregistered color and thermal imagery

Modality	AP <sup>†</sup> <sub>all</sub>	AP <sub>small</sub>	AP <sub>med</sub>	AP <sub>large</sub>	Method	Color	Color (gray)	Color (jitter)	Thermal
Thermal	0.018	0.007	0.022	0.204	SAM [33] + GT ann. <sup>‡</sup>	0.704	0.698	0.700	0.653
Color (grayscale)	0.538	0.536	0.531	0.601	Grounded SAM [43]	0.380	0.351	0.361	0.193
Color (col. jitter)	0.800	0.792	0.801	0.841	OV-Seg [38]	0.362	0.340	0.365	0.217
					ODISE [77]	0.504	0.450	0.486	0.232

<sup>†</sup>refers to AP@0.5::0.95, following MSCOCO [40] <sup>‡</sup> Most frequent ground truth class label in a SAM mask assigned as label for entire mask

### 4.5 Further Analysis

**Zero-shot foundation models on thermal imagery** Current foundation models work well on RGB imagery but have not been benchmarked on thermal, especially in non-urban settings. To evaluate these models on thermal imagery, specifically for zero-shot segmentation and semantic segmentation, we compare RGB and thermal performance using the aligned set (Sec. 3.2) in order to isolate modality as the root cause for performance differences. In the following tests, our metrics do not include the rare *object* classes (*vehicle, person*) as they drop metrics to near-uniform values for both modalities, making it difficult to compare.

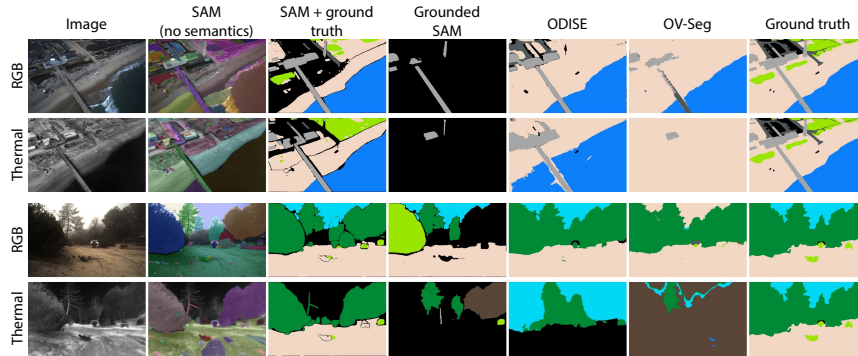


**Fig. 7:** Zero-shot foundation models on RGB-T pairs. Oversegmented SAM outputs differ across modalities but are similar with ground truth semantics added. Semantic segmentation models (prompted with all classes) perform better on RGB imagery.

We quantify Segment Anything’s (SAM) [33] zero-shot segmentation sensitivity to modality change by measuring the spatial alignment of its mask outputs. We apply it to the RGB set and the 8-bit thermal image set (Sec. 3.2) with the default  $32 \times 32$  grid points to segment everything (Fig. 7). We compute the average precision (AP) of the predicted thermal masks, using the predicted RGB masks as ground truth, and compare the thermal AP to the APs of a color-jittered RGB set and a grayscale set. We find that SAM is sensitive to photometric changes, with large performance drops from color-jitter to grayscale to thermal (Tab. 7a).

Next, we test large vision-language models (Grounded-SAM [43], OV-Seg [38], and ODISE [77]) in zero-shot semantic segmentation. We prompt the models

with a list of classes in our dataset; generate semantic segmentation masks for RGB, color-jittered RGB, grayscale, and thermal image sets; and compute the mIoU of their outputs using our ground truth annotations. Although RGB, RGB-variants, and thermal modalities all yield poor semantic segmentation performance (Tab. 7b), all RGB variants outperform thermal by at least 0.13 mIoU, indicating low generalization to the thermal modality (Fig. 7).

Finally, we create semantic SAM masks by assigning class labels to SAM instances based on the most frequent ground truth class within an instance (Fig. 7). We find that these masks attain much higher mIoU score (0.653) compared to the other zero-shot methods. Based on the results (Tab. 7), we note that SAM can find object boundaries in the thermal domain reasonably well but can over-segment, resulting in poor AP scores when compared to RGB (which can also oversegment). When taken with ground truth semantics, this behavior is hidden.

**Transfer learning with urban thermal datasets** We test if pre-training on thermal urban data can assist transfer to field settings. We sample 40k unlabeled thermal images from [11, 17, 22, 41, 61, 67, 71, 76] and pretrain various networks using Mo-

CoV2 [9]. We then finetune the pretrained networks on our training set and evaluate on our test set. Overall, we find sparse evidence suggesting any advantage of pretraining with existing urban thermal datasets (Tab. 8). Off-the-shelf ImageNet weights can provide strong performance in the thermal field domain, especially over training from scratch, without the effort and costs of pretraining.

## 5 Conclusion

We presented the Caltech Aerial RGB-Thermal Dataset, the first dataset tailored towards advancing thermal semantic perception and motion tracking algorithms in natural environments. We created four benchmarks encompassing semantic segmentation, image translation, and motion tracking, and demonstrate challenges faced by current thermal perception and localization algorithms. Semantic segmentation and image translation methods were notably affected by geographical domain shifts, reflecting the wide intra-class and inter-scenery distributions in our dataset, and temporal domain shifts, due to thermal inversion and crossover. Motion tracking in thermal suffered from feature sparsity, a challenge commonly encountered in real-world robotic deployments [1]. Our motion tracking benchmark penalizes current VIO/SLAM algorithms for assuming ideal feature-tracking conditions, serving as a testbed to fuel improvements in this area. Our dataset and benchmarks can be used into the future to help develop algorithms that expand the operating domains of robotics and computer vision.

## Acknowledgements

This work was funded by the Office of Naval Research. We thank K. Koetje, K. Brodie, T. Hesser, T. Almeida, T. Cook, N. Spore, and R. Beach.

**Table 8:** Network pretraining methods for downstream thermal segmentation.

Model	mIoU			# Params. (M)
	None	ImageNet	Therm. Urban	
FastSCNN	0.640	0.690	0.688	1.1
EfficientViT	0.687	0.725	0.714	4.8
ResNet18	0.702	0.713	0.706	12.3
ResNet50	0.682	0.713	0.728	26.7
ConvNext-B	0.625	0.717	0.697	89.4

## References

1. Ackerman, E.: Blade strike on landing ends mars helicopter’s epic journey (Jan 2024), <https://spectrum.ieee.org/mars-helicopter-ingenuity-end-mission>
2. Bloesch, M., Burri, M., Omari, S., Hutter, M., Siegwart, R.: Iterated extended kalman filter based visual-inertial odometry using direct photometric feedback. *The International Journal of Robotics Research* **36**(10), 1053–1072 (2017)
3. Bondi, E., Jain, R., Aggrawal, P., Anand, S., Hannaford, R., Kapoor, A., Piavis, J., Shah, S., Joppa, L., Dilkina, B., et al.: Birdsai: A dataset for detection and tracking in aerial thermal infrared videos. In: *Proceedings of the IEEE/CVF Winter Conference on Applications of Computer Vision*. pp. 1747–1756 (2020)
4. Brodie, K.L., Bruder, B.L., Slocum, R.K., Spore, N.J.: Simultaneous mapping of coastal topography and bathymetry from a lightweight multicamera uas. *IEEE Transactions on Geoscience and Remote Sensing* **57**(9), 6844–6864 (2019). <https://doi.org/10.1109/TGRS.2019.2909026>
5. Cai, H., Gan, C., Han, S.: Efficientvit: Enhanced linear attention for high-resolution low-computation visual recognition. *arXiv preprint arXiv:2205.14756* (2022)
6. Cai, W., Jin, K., Hou, J., Guo, C., Wu, L., Yang, W.: Vdd: Varied drone dataset for semantic segmentation. *arXiv preprint arXiv:2305.13608* (2023)
7. Center, A.F.S.: A dataset for machine learning algorithm development from 2010-06-15 to 2010-08-15. NOAA National Centers for Environmental Information (2019)
8. Chen, L.C., Zhu, Y., Papandreou, G., Schroff, F., Adam, H.: Encoder-decoder with atrous separable convolution for semantic image segmentation. In: *Proceedings of the European conference on computer vision (ECCV)*. pp. 801–818 (2018)
9. Chen, X., Fan, H., Girshick, R., He, K.: Improved baselines with momentum contrastive learning. *arXiv preprint arXiv:2003.04297* (2020)
10. Chen, Y., Wang, Y., Lu, P., Chen, Y., Wang, G.: Large-scale structure from motion with semantic constraints of aerial images. In: *Pattern Recognition and Computer Vision: First Chinese Conference, PRCV 2018, Guangzhou, China, November 23-26, 2018, Proceedings, Part I 1*. pp. 347–359. Springer (2018)
11. Choi, Y., Kim, N., Hwang, S., Park, K., Yoon, J.S., An, K., Kweon, I.S.: Kaist multi-spectral day/night data set for autonomous and assisted driving. *IEEE Transactions on Intelligent Transportation Systems* **19**(3), 934–948 (2018)
12. Deevi, S.A., Lee, C., Gan, L., Nagesh, S., Pandey, G., Chung, S.J.: Rgb-x object detection via scene-specific fusion modules. In: *Proceedings of the IEEE/CVF Winter Conference on Applications of Computer Vision*. pp. 7366–7375 (2024)
13. Delaune, J., Hewitt, R., Lytle, L., Sorice, C., Thakker, R., Matthies, L.: Thermal-inertial odometry for autonomous flight throughout the night. In: *2019 IEEE/RSJ International Conference on Intelligent Robots and Systems (IROS)*. pp. 1122–1128. IEEE (2019)
14. Doer, C., Trommer, G.F.: Radar visual inertial odometry and radar thermal inertial odometry: Robust navigation even in challenging visual conditions. In: *2021 IEEE/RSJ International Conference on Intelligent Robots and Systems (IROS)*. pp. 331–338. IEEE (2021)
15. Esser, P., Rombach, R., Ommer, B.: Taming transformers for high-resolution image synthesis. In: *Proceedings of the IEEE/CVF conference on computer vision and pattern recognition*. pp. 12873–12883 (2021)
16. Feng, D., Haase-Schütz, C., Rosenbaum, L., Hertlein, H., Glaeser, C., Timm, F., Wiesbeck, W., Dietmayer, K.: Deep multi-modal object detection and semantic

- segmentation for autonomous driving: Datasets, methods, and challenges. *IEEE Transactions on Intelligent Transportation Systems* **22**(3), 1341–1360 (2020)
17. Teledyne flir adas dataset, <https://www.flir.com/oem/adas/adas-dataset-form/>, Last accessed on 2023-10-27
  18. Fountas, S., Mylonas, N., Malounas, I., Rodias, E., Hellmann Santos, C., Pekkeriet, E.: Agricultural robotics for field operations. *Sensors* **20**(9), 2672 (2020)
  19. Gade, R., Moeslund, T.B.: Thermal cameras and applications: a survey. *Machine vision and applications* **25**, 245–262 (2014)
  20. Gan, L., Lee, C., Chung, S.J.: Unsupervised rgb-to-thermal domain adaptation via multi-domain attention network. In: 2023 IEEE International Conference on Robotics and Automation (ICRA). pp. 6014–6020. IEEE (2023)
  21. Geneva, P., Ekenhoff, K., Lee, W., Yang, Y., Huang, G.: Openvins: A research platform for visual-inertial estimation. In: 2020 IEEE International Conference on Robotics and Automation (ICRA). pp. 4666–4672. IEEE (2020)
  22. Ha, Q., Watanabe, K., Karasawa, T., Ushiku, Y., Harada, T.: Mfnet: Towards real-time semantic segmentation for autonomous vehicles with multi-spectral scenes. In: 2017 IEEE/RSJ International Conference on Intelligent Robots and Systems (IROS). pp. 5108–5115. IEEE (2017)
  23. He, K., Zhang, X., Ren, S., Sun, J.: Deep residual learning for image recognition. In: Proceedings of the IEEE conference on computer vision and pattern recognition. pp. 770–778 (2016)
  24. He, M., Rajkumar, R.R.: Using thermal vision for extended vins-mono to localize vehicles in large-scale outdoor road environments. In: 2021 IEEE Intelligent Vehicles Symposium (IV). pp. 953–960. IEEE (2021)
  25. Howard, A., Sandler, M., Chu, G., Chen, L.C., Chen, B., Tan, M., Wang, W., Zhu, Y., Pang, R., Vasudevan, V., et al.: Searching for mobilenetv3. In: Proceedings of the IEEE/CVF international conference on computer vision. pp. 1314–1324 (2019)
  26. Hua, T., Pei, L., Li, T., Wu, Q., Wang, R., Yu, W.: I2-slam: Fusing infrared camera and imu for simultaneous localization and mapping. In: International Conference on Autonomous Unmanned Systems. pp. 2834–2844. Springer (2021)
  27. Huang, X., Liu, M.Y., Belongie, S., Kautz, J.: Multimodal unsupervised image-to-image translation. In: European Conference on Computer Vision (ECCV) (2018)
  28. Isola, P., Zhu, J.Y., Zhou, T., Efros, A.A.: Image-to-image translation with conditional adversarial networks. In: Proceedings of the IEEE conference on computer vision and pattern recognition. pp. 1125–1134 (2017)
  29. Jia, X., Zhu, C., Li, M., Tang, W., Zhou, W.: Llvip: A visible-infrared paired dataset for low-light vision. In: Proceedings of the IEEE/CVF International Conference on Computer Vision. pp. 3496–3504 (2021)
  30. Jong, A., Yu, M., Dhrafani, D., Kailas, S., Moon, B., Sycara, K., Scherer, S.: Wit-uas: A wildland-fire infrared thermal dataset to detect crew assets from aerial views. In: 2023 IEEE/RSJ International Conference on Intelligent Robots and Systems (IROS). pp. 11464–11471. IEEE (2023)
  31. Khattak, S., Papachristos, C., Alexis, K.: Keyframe-based direct thermal-inertial odometry. In: 2019 International Conference on Robotics and Automation (ICRA). pp. 3563–3569. IEEE (2019)
  32. Kim, Y.H., Shin, U., Park, J., Kweon, I.S.: Ms-uda: Multi-spectral unsupervised domain adaptation for thermal image semantic segmentation. *IEEE Robotics and Automation Letters* **6**(4), 6497–6504 (Oct 2021). <https://doi.org/10.1109/LRA.2021.3093652>

33. Kirillov, A., Mintun, E., Ravi, N., Mao, H., Rolland, C., Gustafson, L., Xiao, T., Whitehead, S., Berg, A.C., Lo, W.Y., Dollár, P., Girshick, R.: Segment anything. arXiv:2304.02643 (2023)
34. Lee, C., Frennert, J.G., Gan, L., Anderson, M., Chung, S.J.: Online self-supervised thermal water segmentation for aerial vehicles. In: 2023 IEEE/RSJ International Conference on Intelligent Robots and Systems (IROS). pp. 7734–7741. IEEE (2023)
35. Lee, D.G., Jeon, M.H., Cho, Y., Kim, A.: Edge-guided multi-domain rgb-to-tir image translation for training vision tasks with challenging labels. In: 2023 IEEE International Conference on Robotics and Automation (ICRA). pp. 8291–8298. IEEE (2023)
36. Li, C., Xia, W., Yan, Y., Luo, B., Tang, J.: Segmenting objects in day and night: Edge-conditioned cnn for thermal image semantic segmentation. *IEEE Transactions on Neural Networks and Learning Systems* **32**(7), 3069–3082 (2020)
37. Li, H., Ma, Y., Huang, Y., Gu, Y., Xu, W., Liu, Y., Zuo, X.: Riders: Radar-infrared depth estimation for robust sensing. arXiv preprint arXiv:2402.02067 (2024)
38. Liang, F., Wu, B., Dai, X., Li, K., Zhao, Y., Zhang, H., Zhang, P., Vajda, P., Marculescu, D.: Open-vocabulary semantic segmentation with mask-adapted clip. In: Proceedings of the IEEE/CVF Conference on Computer Vision and Pattern Recognition. pp. 7061–7070 (2023)
39. Liang, M., Hu, J., Bao, C., Feng, H., Deng, F., Lam, T.L.: Explicit attention-enhanced fusion for rgb-thermal perception tasks. *IEEE Robotics and Automation Letters* (2023)
40. Lin, T.Y., Maire, M., Belongie, S., Hays, J., Perona, P., Ramanan, D., Dollár, P., Zitnick, C.L.: Microsoft coco: Common objects in context. In: Computer Vision–ECCV 2014: 13th European Conference, Zurich, Switzerland, September 6–12, 2014, Proceedings, Part V 13. pp. 740–755. Springer (2014)
41. Liu, J., Fan, X., Huang, Z., Wu, G., Liu, R., Zhong, W., Luo, Z.: Target-aware dual adversarial learning and a multi-scenario multi-modality benchmark to fuse infrared and visible for object detection. In: Proceedings of the IEEE/CVF Conference on Computer Vision and Pattern Recognition. pp. 5802–5811 (2022)
42. Liu, M.Y., Breuel, T., Kautz, J.: Unsupervised image-to-image translation networks. In: Conference on Neural Information Processing Systems (NeurIPS) (2017)
43. Liu, S., Zeng, Z., Ren, T., Li, F., Zhang, H., Yang, J., Li, C., Yang, J., Su, H., Zhu, J., et al.: Grounding dino: Marrying dino with grounded pre-training for open-set object detection. arXiv preprint arXiv:2303.05499 (2023)
44. Liu, Z., Mao, H., Wu, C.Y., Feichtenhofer, C., Darrell, T., Xie, S.: A convnet for the 2020s. In: Proceedings of the IEEE/CVF conference on computer vision and pattern recognition. pp. 11976–11986 (2022)
45. Lyu, Y., Vosselman, G., Xia, G.S., Yilmaz, A., Yang, M.Y.: Uavid: A semantic segmentation dataset for uav imagery. *ISPRS Journal of Photogrammetry and Remote Sensing* **165**, 108 – 119 (2020). <https://doi.org/https://doi.org/10.1016/j.isprsjprs.2020.05.009>, <http://www.sciencedirect.com/science/article/pii/S0924271620301295>
46. Mehta, S., Rastegari, M.: Separable self-attention for mobile vision transformers. arXiv preprint arXiv:2206.02680 (2022)
47. Mostegel, C., Maurer, M., Heran, N., Pestana Puerta, J., Fraundorfer, F.: Semantic drone dataset (Jan 2019), <http://dronedataset.icg.tugraz.at/>, Last accessed on 2023-10-27
48. Nigam, I., Huang, C., Ramanan, D.: Ensemble knowledge transfer for semantic segmentation. In: 2018 IEEE Winter Conference on Applications of Computer Vision (WACV). pp. 1499–1508. IEEE (2018)

49. Nirgudkar, S., DeFilippo, M., Sacarny, M., Benjamin, M., Robinette, P.: Massmind: Massachusetts maritime infrared dataset. *The International Journal of Robotics Research* **42**(1-2), 21–32 (2023)
50. Oquab, M., Darcet, T., Moutakanni, T., Vo, H.V., Szafraniec, M., Khalidov, V., Fernandez, P., Haziza, D., Massa, F., El-Nouby, A., Howes, R., Huang, P.Y., Xu, H., Sharma, V., Li, S.W., Galuba, W., Rabbat, M., Assran, M., Ballas, N., Synnaeve, G., Misra, I., Jegou, H., Mairal, J., Labatut, P., Joulin, A., Bojanowski, P.: Dinov2: Learning robust visual features without supervision (2023)
51. Panetta, K., Shreyas Kamath, K.M., Rajeev, S., Agaian, S.S.: Ftinet: Feature transverse network for thermal image semantic segmentation. *IEEE Access* **9**, 145212–145227 (2021). <https://doi.org/10.1109/ACCESS.2021.3123066>
52. Park, T., Efros, A.A., Zhang, R., Zhu, J.Y.: Contrastive learning for unpaired image-to-image translation. In: *Computer Vision–ECCV 2020: 16th European Conference, Glasgow, UK, August 23–28, 2020, Proceedings, Part IX* 16. pp. 319–345. Springer (2020)
53. Poudel, R., Liwicki, S., Cipolla, R.: Fast-scnn: Fast semantic segmentation network. In: Sidorov, K., Hicks, Y. (eds.) *Proceedings of the British Machine Vision Conference (BMVC)*. pp. 187.1–187.12. BMVA Press (September 2019). <https://doi.org/10.5244/C.33.187>, <https://dx.doi.org/10.5244/C.33.187>
54. Qin, T., Li, P., Shen, S.: Vins-mono: A robust and versatile monocular visual-inertial state estimator. *IEEE Transactions on Robotics* **34**(4), 1004–1020 (2018)
55. Radford, A., Kim, J.W., Hallacy, C., Ramesh, A., Goh, G., Agarwal, S., Sastry, G., Askell, A., Mishkin, P., Clark, J., et al.: Learning transferable visual models from natural language supervision. In: *International conference on machine learning*. pp. 8748–8763. PMLR (2021)
56. Retief, S.P., Willers, C., Wheeler, M.: Prediction of thermal crossover based on imaging measurements over the diurnal cycle. In: *Geo-Spatial and Temporal Image and Data Exploitation III*. vol. 5097, pp. 58–69. SPIE (2003)
57. Rombach, R., Blattmann, A., Lorenz, D., Esser, P., Ommer, B.: High-resolution image synthesis with latent diffusion models. In: *Proceedings of the IEEE/CVF Conference on Computer Vision and Pattern Recognition (CVPR)*. pp. 10684–10695 (June 2022)
58. Saharia, C., Chan, W., Chang, H., Lee, C., Ho, J., Salimans, T., Fleet, D., Norouzi, M.: Palette: Image-to-image diffusion models. In: *ACM SIGGRAPH 2022 Conference Proceedings*. pp. 1–10 (2022)
59. Saputra, M.R.U., Lu, C.X., de Gusmao, P.P.B., Wang, B., Markham, A., Trigoni, N.: Graph-based thermal-inertial slam with probabilistic neural networks. *IEEE Transactions on Robotics* **38**(3), 1875–1893 (2022)
60. Shin, U., Lee, K., Kweon, I.S.: Complementary random masking for rgb-thermal semantic segmentation. In: *IEEE International Conference on Robotics and Automation* (2024)
61. Shin, U., Park, J., Kweon, I.S.: Deep depth estimation from thermal image. In: *Proceedings of the IEEE/CVF Conference on Computer Vision and Pattern Recognition*. pp. 1043–1053 (2023)
62. Shivakumar, S.S., Rodrigues, N., Zhou, A., Miller, I.D., Kumar, V., Taylor, C.J.: Pst900: Rgb-thermal calibration, dataset and segmentation network. In: *2020 IEEE international conference on robotics and automation (ICRA)*. pp. 9441–9447. IEEE (2020)
63. Speth, S., Goncalves, A., Rigault, B., Suzuki, S., Bouazizi, M., Matsuo, Y., Prendinger, H.: Deep learning with rgb and thermal images onboard a drone for monitoring operations. *Journal of Field Robotics* **39**(6), 840–868 (2022)

64. Sturm, J., Engelhard, N., Endres, F., Burgard, W., Cremers, D.: A benchmark for the evaluation of rgb-d slam systems. In: 2012 IEEE/RSJ international conference on intelligent robots and systems. pp. 573–580. IEEE (2012)
65. Sun, Y., Zuo, W., Liu, M.: Rtfnet: Rgb-thermal fusion network for semantic segmentation of urban scenes. *IEEE Robotics and Automation Letters* **4**(3), 2576–2583 (2019). <https://doi.org/10.1109/LRA.2019.2904733>
66. Sun, Y., Zuo, W., Yun, P., Wang, H., Liu, M.: Fuseseg: Semantic segmentation of urban scenes based on rgb and thermal data fusion. *IEEE Transactions on Automation Science and Engineering* **18**(3), 1000–1011 (2021). <https://doi.org/10.1109/TASE.2020.2993143>
67. Suo, J., Wang, T., Zhang, X., Chen, H., Zhou, W., Shi, W.: Hit-uav: A high-altitude infrared thermal dataset for unmanned aerial vehicle-based object detection. *Scientific Data* **10**, 227 (2023)
68. Tan, M., Le, Q.: Efficientnet: Rethinking model scaling for convolutional neural networks. In: International conference on machine learning. pp. 6105–6114. PMLR (2019)
69. Ustun, B., Kaya, A.K., Ayerden, E.C., Altinel, F.: Spectral transfer guided active domain adaptation for thermal imagery. In: Proceedings of the IEEE/CVF Conference on Computer Vision and Pattern Recognition (CVPR) Workshops. pp. 449–458 (June 2023)
70. Vargas, J., Alswiss, S., Toker, O., Razdan, R., Santos, J.: An overview of autonomous vehicles sensors and their vulnerability to weather conditions. *Sensors* **21**(16), 5397 (2021)
71. Vertens, J., Zürn, J., Burgard, W.: Heatnet: Bridging the day-night domain gap in semantic segmentation with thermal images. In: 2020 IEEE/RSJ International Conference on Intelligent Robots and Systems (IROS). pp. 8461–8468. IEEE (2020)
72. VS, V., Poster, D., You, S., Hu, S., Patel, V.M.: Meta-uda: Unsupervised domain adaptive thermal object detection using meta-learning. In: Proceedings of the IEEE/CVF Winter Conference on Applications of Computer Vision (WACV). pp. 1412–1423 (January 2022)
73. Wang, T.C., Liu, M.Y., Zhu, J.Y., Tao, A., Kautz, J., Catanzaro, B.: High-resolution image synthesis and semantic manipulation with conditional gans. In: Proceedings of the IEEE Conference on Computer Vision and Pattern Recognition (2018)
74. Xie, E., Wang, W., Yu, Z., Anandkumar, A., Alvarez, J.M., Luo, P.: Segformer: Simple and efficient design for semantic segmentation with transformers. In: Neural Information Processing Systems (NeurIPS) (2021)
75. Xie, S., Girshick, R., Dollár, P., Tu, Z., He, K.: Aggregated residual transformations for deep neural networks. In: Proceedings of the IEEE conference on computer vision and pattern recognition. pp. 1492–1500 (2017)
76. Xiong, H., Cai, W., Liu, Q.: Mcnet: Multi-level correction network for thermal image semantic segmentation of nighttime driving scene. *Infrared Physics & Technology* p. 103628 (2021). <https://doi.org/https://doi.org/10.1016/j.infrared.2020.103628>
77. Xu, J., Liu, S., Vahdat, A., Byeon, W., Wang, X., De Mello, S.: Open-vocabulary panoptic segmentation with text-to-image diffusion models. In: Proceedings of the IEEE/CVF Conference on Computer Vision and Pattern Recognition. pp. 2955–2966 (2023)
78. Yun, S., Jung, M., Kim, J., Jung, S., Cho, Y., Jeon, M.H., Kim, G., Kim, A.: Sthereo: Stereo thermal dataset for research in odometry and mapping. In: 2022

- IEEE/RSJ International Conference on Intelligent Robots and Systems (IROS). pp. 3857–3864. IEEE (2022)
79. Zhang, J., Liu, R., Shi, H., Yang, K., Reiß, S., Peng, K., Fu, H., Wang, K., Stiefelhagen, R.: Delivering arbitrary-modal semantic segmentation. In: CVPR (2023)
  80. Zhao, S., Wang, P., Zhang, H., Fang, Z., Scherer, S.: Tp-tio: A robust thermal-inertial odometry with deep thermalpoint. In: 2020 IEEE/RSJ International Conference on Intelligent Robots and Systems (IROS). pp. 4505–4512. IEEE (2020)
  81. Zhou, W., Liu, J., Lei, J., Yu, L., Hwang, J.N.: Gmnet: Graded-feature multilabel-learning network for rgb-thermal urban scene semantic segmentation. IEEE Transactions on Image Processing **30**, 7790–7802 (2021). <https://doi.org/10.1109/TIP.2021.3109518>
  82. Zhu, J.Y., Park, T., Isola, P., Efros, A.A.: Unpaired image-to-image translation using cycle-consistent adversarial networks. In: Proceedings of the IEEE international conference on computer vision. pp. 2223–2232 (2017)
  83. Zhu, P., Wen, L., Du, D., Bian, X., Fan, H., Hu, Q., Ling, H.: Detection and tracking meet drones challenge. IEEE Transactions on Pattern Analysis and Machine Intelligence **44**(11), 7380–7399 (2021)



# Caltech Aerial RGB-Thermal Dataset in the Wild Supplementary Material

Connor Lee\*, Matthew Anderson\*, Nikhil Raganathan, Xingxing Zuo,  
Kevin Do, Georgia Gkioxari, and Soon-Jo Chung

California Institute of Technology

{clee, matta, nrangana, zuox, kdo, georgia, sjchung}@caltech.edu

## S1 Comparison of Related Benchmarks and Datasets

A detailed comparison of related datasets and benchmarks is shown in Tab. S1. Included datasets must be captured from aerial vehicles, surface vehicles (boats), or cars. We included pure RGB datasets only if they are related to semantic segmentation or object detection and captured from aerial vehicles. Other datasets included for comparison must contain thermal imagery and be related to semantic segmentation or object detection.

**Table S1:** Comparison of datasets captured from aerial platforms or depicting thermal scenes.

Dataset	Platform	Task	RGB	Thermal	GPS	IMU	Setting	Location	# Samples	Camera pose
<b>Ours</b>	UAV	Sem. Seg.	✓	✓	✓	✓	River, Coast, Lake, Mountain, Desert	USA	4,195	20°, 45°, < 120 m
AeroScapes [26], UDD [4], UAVid [23], VDD [3], IDD [3]	UAV	Sem. Seg.	✓	✗	✗	✗	Urban	China	205 - 3269	30 - 90°, < 100 m
Semantic Drone Dataset [25]	UAV	Sem. Seg.	✓	✓	✗	✓	Urban	Germany	400	90°, < 30m
Swiss and Okutama Drone Datasets [37]	UAV	Sem. Seg.	✓	✗	✗	✗	Urban	Switzerland, Japan	191	90°
NILCU Multispectral Aerial Person Detection [37]	UAV	Person Det.	✓	✓	✗	✗	Urban	Japan	5,880	45°
WIT-UAS [16]	UAV	Obj. Det.	✗	✓	✓	✓	Forest	USA	6,951	30°, 90°, < 120 m
VisDrone [47]	UAV	Obj. Det.	✓	✗	✗	✗	Urban	China	10,209	Variable
MassMIND [27]	USV	Sem. Seg.	✗	✓	✓	✓	Harbor	USA	2,900	0°, 0 m
Flir ADAS [7]	Car	Obj. Det.	✓	✓	✗	✗	Urban	USA	10,228	0°, 0 m
BIRDSAI [1]	UAV	Obj. Track.	✗	✓	✗	✗	Savannas	S. Africa	62,000	Off-nadir, 60-120 m
HIT-UAV [38]	UAV	Obj. Det.	✓	✓	✗	✗	Urban	China	2,898	30°-90°, 60-130 m
KAIST Multispectral [5]	Car	Obj. Det.	✓	✓	✓	✓	Urban	S. Korea	4750	0°, 0 m
MFNet [10]	Car	Sem. Seg.	✓	✓	✗	✗	Urban	Japan	1,569	0°, 0 m
M <sup>3</sup> FD [29]	Car	Obj. Det.	✓	✓	✗	✗	Urban	China	4,200	0°, 0 m
Freiburg Thermal [40]	Car	Sem. Seg.	✓	✓	✗	✗	Urban	Germany	20,656 <sup>†</sup>	0°, 0 m
SODA [18], SCUT-Seg [44]	Car	Sem. Seg.	✗	✓	✗	✗	Indoor/Urban	—	~2,000	0°, 0 m
STherEO [45], MS <sup>2</sup> [35]	Car	SLAM / Depth Est.	✓	✓	✓	✓	Urban/Suburban	S. Korea	—	0°, 0 m
PST900 [36]	UGV	Sem. Seg.	✓	✓	✗	✗	Subterranean	USA	894	0°, 0 m
LLVIP [15]	Building (fixed)	Pedestrian Detection	✓	✓	✗	✗	Urban	China	14,588	Variable

<sup>†</sup> Camera angle of 90° is nadir-pointing    <sup>‡</sup> Annotations provided for only 64 test set images.

\* These authors contributed equally to this work.

## S2 Dataset Information

Our dataset consists of 37 aerial and ground trajectories captured from diverse natural landscapes across the USA. Further details are shown in Tab. S2. Visualizations of several flight trajectories are shown in Fig. S1.

**Table S2:** Dataset capture locations and settings.

Location of Capture	Terrain Type	Capture Method	Motion	Time of Day	# Seq.	Total Time
Kentucky River, KY	River	UAV Flight	Large	Afternoon	3	17m10s
Colorado River, CA	River	UAV Flight	Large	Sunrise	4	32m50s
Castaic Lake, CA	Lake	UAV Flight	Large	Midday	4	58m56s
Duck, NC	Coast	UAV Flight	Large	Day/Night	7	91m26s
Big Bear Lake, CA	Lake	Ground	Minor	Mid-morning	8	15m52s
Arroyo Seco, CA	Stream	Ground	Still	Afternoon	8	10m22s
Idyllwild, CA	Mountain	Ground	Minor	Day	2	5m58s
Joshua Tree, CA	Desert	Ground	Minor	Day	2	5m58s
North Field (Caltech), CA	Urban	UAV Flight	Large	Day	5	26m13s

### S2.1 Data Capture

All data is stored as ROS1 rosbags as this is a natural format for robotics work. As the rosbag format may not be preferred for all users, extraction tools for generating csv and images files are provided at *link\_provided\_after\_review*. Within the rosbags, the synchronized data contains timestamps for both the time of trigger (*sync/rate\_\**) and time the data was received (header stamp in the topic), allowing the data to be aligned in post-processing regardless of transport delays in the system. Where available, position data should be taken from the UAV (*uav1/mavros/local\_position/\** topics) and orientation data from the VN100 (*imu/imu*) to provide the best available estimate. Finally, while mostly complete, not all datasets contain all sensors due to issues when collecting data.

### S2.2 Sensor Calibration

We calibrate the three cameras and IMU via Kalibr [8] by conducting three independent calibrations. We do this to isolate any difficulties caused by the thermal camera. We first calibrate the thermal camera and IMU, and then perform stereo calibration for each possible camera pairing. Thermal calibrations are done using a 10×10 circle grid (1" diameter). To ensure calibration image sharpness in the thermal domain, we place the calibration board in direct sunlight for 2-3 minutes prior to data collection and keep it illuminated (reflecting sunlight) during the entire collection process. The RGB and Mono cameras were calibrated using a standard 6x6 April tag grid board.

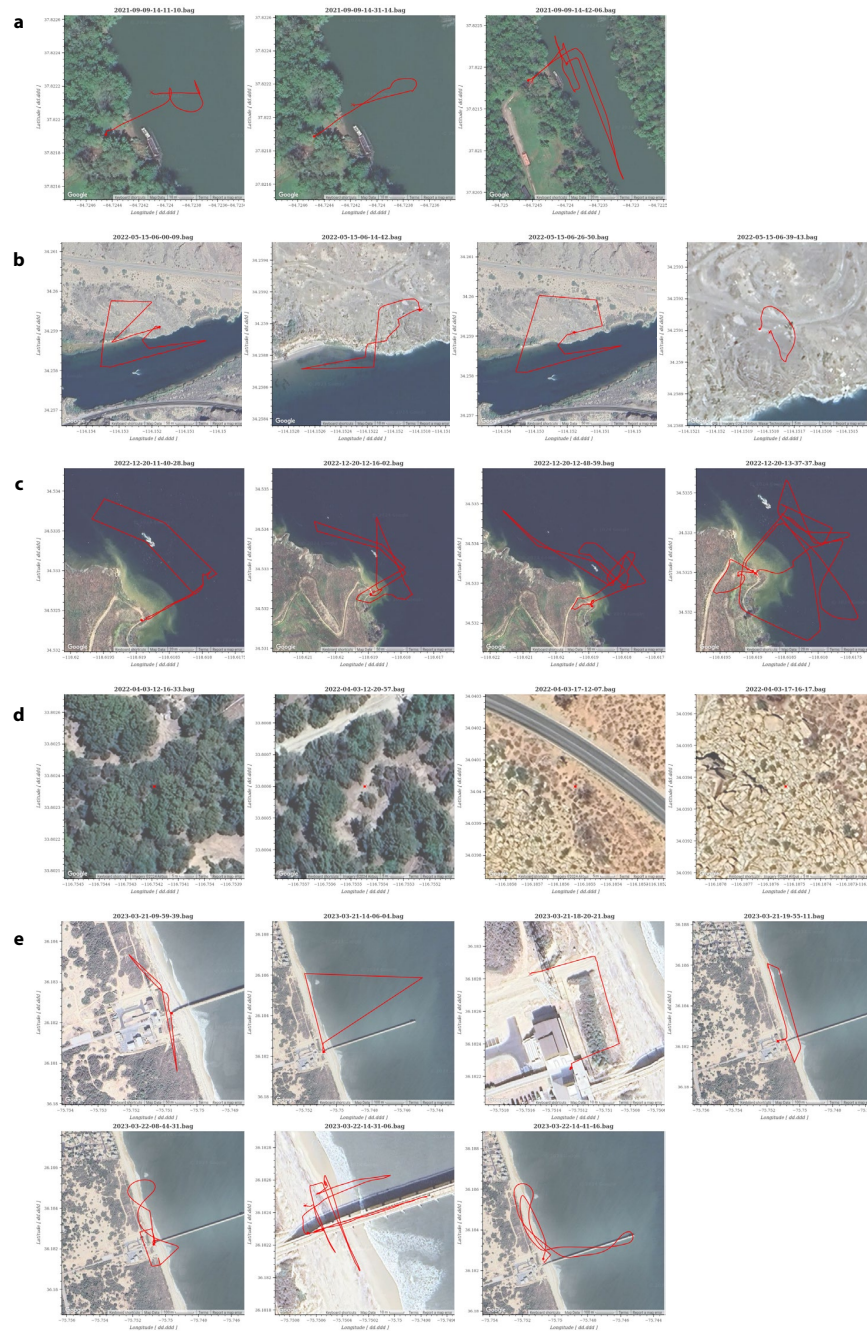


**Fig.S1:** Trajectories from our dataset: (a) Kentucky River (b) Colorado River (c) Castaic Lake (d) Idyllwild and Joshua Tree (e) Duck. North Field trajectories not shown.

### S2.3 Labeling Process for Semantic Segmentation Annotations

The thermal images were labeled via manual annotation. Annotators were asked to read a guide with descriptions of each trajectory. Descriptions contained lists of possible classes, a expert-labeled examples provided by the authors, and GPS coordinates (for look-up in Google Earth). During labeling, annotators were presented with a side-by-side copy of a thermal image and its corresponding RGB image, the trajectory it came from, and were asked to annotate the thermal image. The annotations were reviewed by authors, with rejected annotations sent back for re-annotation. A total of 3 rounds of annotation were conducted.

## S3 Implementation and Training Details

Our baselines were implemented using code from public Github repositories shown in Tab. S3. Official code was used whenever possible. We trained and tested all networks using a single Nvidia A6000 ADA GPU (48 GB).

**Table S3:** Public repositories used in this work to create our baselines

Baselines	Public Repositories
<b>Thermal Segmentation</b>	
FastSCNN [31]	Tramac/Fast-SCNN-pytorch
EfficientViT [2]	mit-han-lab/efficientvit
Segformer [42]	NVlabs/SegFormer
DINOv2 [28]	facebookresearch/dinov2
FTNet [29]	shreyaskamathkm/FTNet
Everything else [11, 12, 22, 24, 39, 43]	huggingface/pytorch-image-models + qubvel/segmentation_models.pytorch
<b>RGB-T Segmentation</b>	
EAEFNet [19]	FreeformRobotics/EAEFNet
CRM [34]	UkcheolShin/CRM_RGBTSeg
CMNeXt [46]	jamycheung/DELIVER
<b>RGB-T Image Translation</b>	
UNIT [21]	NVlabs/imaginaire
MUNIT [13]	NVlabs/imaginaire
Edge-guided RGB-T [17]	RPM-Robotics-Lab/sRGB-TIR
Pix2Pix [14]	junyanz/pytorch-CycleGAN-and-pix2pix
Pix2PixHD [41]	NVIDIA/pix2pixHD
VQ-GAN [6]	CompVis/taming-transformers
Palette [33]	Janspiry/Palette-Image-to-Image-Diffusion-Models
<b>VIO/SLAM</b>	
VINS-Fusion [32]	HKUST-Aerial-Robotics/VINS-Fusion
OpenVINS [9]	rpng/open_vins

### S3.1 Thermal Baselines

Most networks used in our thermal baseline experiments (Tab. 2) employed a DeepLabV3+ segmentation head with the exception of FastSCNN [31], EfficientViT [2], Segformer [42], DINOv2, and FTNet. For DINOv2, we implemented the linear and nonlinear multi-scale segmentation heads ourselves, with their architectures shown in Tab. S4. All networks, besides DINOv2 and ConvNeXt (CLIP), were trained starting from pretrained ImageNet weights.

**Table S4:** Multi-scale segmentation head architecture used with DINOv2. The architecture is described using PyTorch syntax [30].

DINOv2 Linear Head	DINOv2 Nonlinear Head
<code>nn.Conv2d(384*4, 10, 1)</code>	<code>nn.Conv2d(384*4, 512, 3, padding=1)</code>
	<code>nn.GELU</code>
	<code>nn.Conv2d(512, 10, 1)</code>

Networks were trained for 300 epochs or until validation loss plateaued. We used the Adam optimizer with a  $1e-3$  learning rate that decayed at an exponential rate of 0.99 and a batch size of 64. We augmented our 16-bit thermal training data using random contrast stretches (within the lower and upper 5<sup>th</sup> percentiles) and CLAHE with a random clip limit (see Sec. 3.2). Photometric augmentations were followed by horizontal flips, rotations (within  $10^\circ$ ), scaling between 1 and 1.5, and random crops to  $512 \times 512$ .

### S3.2 RGB-T Segmentation, Image Translation, and VIO/SLAM

We used the repositories listed in Tab. S3 and followed their training procedures. However, we increased the batch size to maximize GPU memory usage whenever possible.

## S4 Additional Results

### S4.1 Relative Thermal Pixel Intensities Throughout the Day

In order to better understand how different objects and entities appear in thermal imagery at different times of day, we plot the thermal pixel intensities of each class (using the ground truth annotations) as a function of their recorded capture time (Fig. S2). Since our thermal camera was not radiometric, we plotted the relative thermal pixel values post-normalization using the normalization scheme described in Sec. 3.2. The plots show cases of thermal inversion between certain classes, notably *bare ground* and *water*.

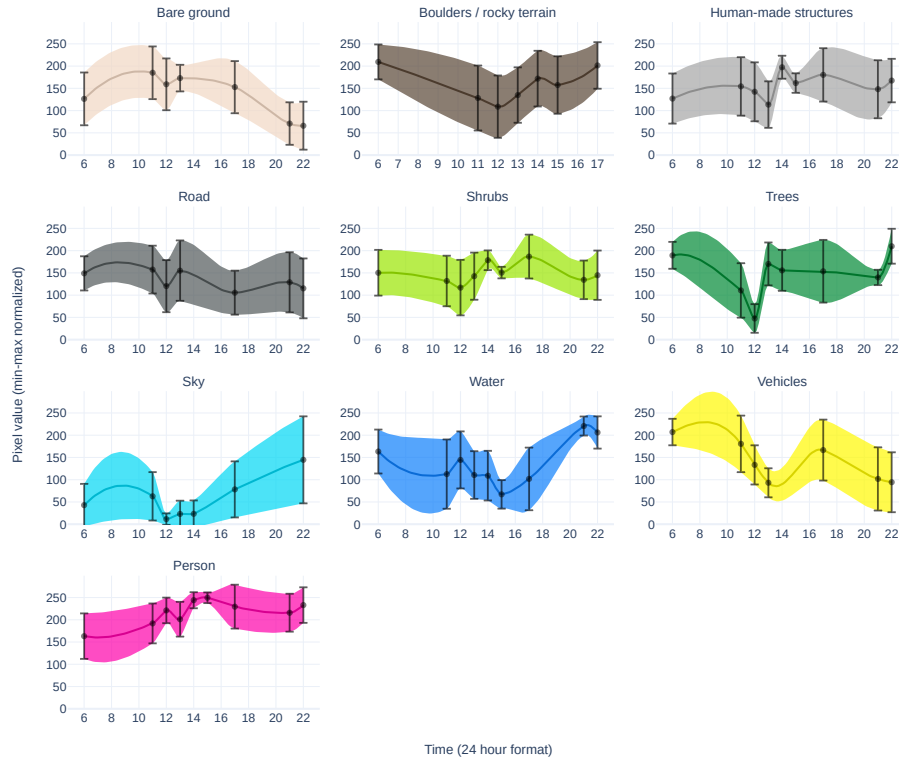


**Fig. S2:** Change in normalized pixel values per class throughout the day.

## S5 Examples

### S5.1 Thermal Inversion

Thermal inversion occurs when object pixel values change depending on its temperature. One notable example of this is thermal inversion of water and land as seen in Fig. S3. In this example, the two images were taken over the same location (Duck, NC) but at different times of day.

## References

1. Bondi, E., Jain, R., Aggrawal, P., Anand, S., Hannaford, R., Kapoor, A., Piavis, J., Shah, S., Joppa, L., Dilkina, B., et al.: Birdsai: A dataset for detection and tracking in aerial thermal infrared videos. In: Proceedings of the IEEE/CVF Winter Conference on Applications of Computer Vision. pp. 1747–1756 (2020)
2. Cai, H., Gan, C., Han, S.: Efficientvit: Enhanced linear attention for high-resolution low-computation visual recognition. arXiv preprint arXiv:2205.14756 (2022)
3. Cai, W., Jin, K., Hou, J., Guo, C., Wu, L., Yang, W.: Vdd: Varied drone dataset for semantic segmentation. arXiv preprint arXiv:2305.13608 (2023)

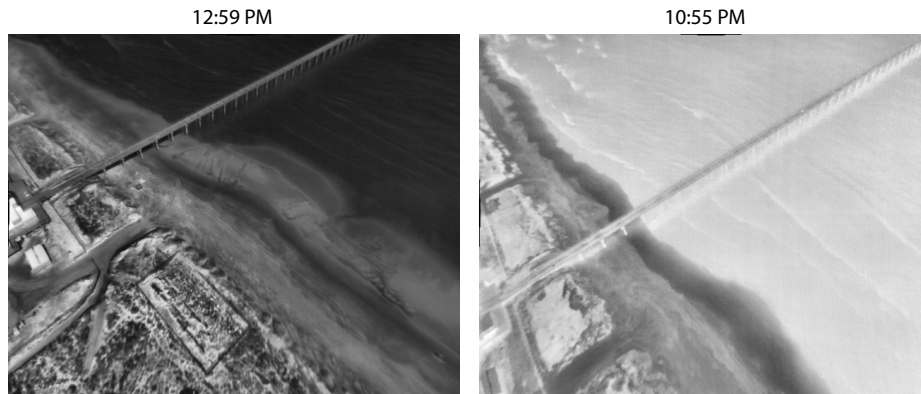


**Fig. S3:** Example of thermal inversion of water and land classes at Duck, NC.

4. Chen, Y., Wang, Y., Lu, P., Chen, Y., Wang, G.: Large-scale structure from motion with semantic constraints of aerial images. In: Pattern Recognition and Computer Vision: First Chinese Conference, PRCV 2018, Guangzhou, China, November 23-26, 2018, Proceedings, Part I 1. pp. 347–359. Springer (2018)
5. Choi, Y., Kim, N., Hwang, S., Park, K., Yoon, J.S., An, K., Kweon, I.S.: Kaist multi-spectral day/night data set for autonomous and assisted driving. *IEEE Transactions on Intelligent Transportation Systems* **19**(3), 934–948 (2018)
6. Esser, P., Rombach, R., Ommer, B.: Taming transformers for high-resolution image synthesis. In: Proceedings of the IEEE/CVF conference on computer vision and pattern recognition. pp. 12873–12883 (2021)
7. Teledyne flir adas dataset, <https://www.flir.com/oem/adas/adas-dataset-form/>, Last accessed on 2023-10-27
8. Furgale, P., Rehder, J., Siegwart, R.: Unified temporal and spatial calibration for multi-sensor systems. In: IEEE/RSJ International Conference on Intelligent Robots and Systems (IROS) (2013)
9. Geneva, P., Eickenhoff, K., Lee, W., Yang, Y., Huang, G.: Openvins: A research platform for visual-inertial estimation. In: 2020 IEEE International Conference on Robotics and Automation (ICRA). pp. 4666–4672. IEEE (2020)
10. Ha, Q., Watanabe, K., Karasawa, T., Ushiku, Y., Harada, T.: Mfnet: Towards real-time semantic segmentation for autonomous vehicles with multi-spectral scenes. In: 2017 IEEE/RSJ International Conference on Intelligent Robots and Systems (IROS). pp. 5108–5115. IEEE (2017)
11. He, K., Zhang, X., Ren, S., Sun, J.: Deep residual learning for image recognition. In: Proceedings of the IEEE conference on computer vision and pattern recognition. pp. 770–778 (2016)
12. Howard, A., Sandler, M., Chu, G., Chen, L.C., Chen, B., Tan, M., Wang, W., Zhu, Y., Pang, R., Vasudevan, V., et al.: Searching for mobilenetv3. In: Proceedings of the IEEE/CVF international conference on computer vision. pp. 1314–1324 (2019)
13. Huang, X., Liu, M.Y., Belongie, S., Kautz, J.: Multimodal unsupervised image-to-image translation. In: European Conference on Computer Vision (ECCV) (2018)

14. Isola, P., Zhu, J.Y., Zhou, T., Efros, A.A.: Image-to-image translation with conditional adversarial networks. In: Proceedings of the IEEE conference on computer vision and pattern recognition. pp. 1125–1134 (2017)
15. Jia, X., Zhu, C., Li, M., Tang, W., Zhou, W.: Llvip: A visible-infrared paired dataset for low-light vision. In: Proceedings of the IEEE/CVF International Conference on Computer Vision. pp. 3496–3504 (2021)
16. Jong, A., Yu, M., Dhrafani, D., Kailas, S., Moon, B., Sycara, K., Scherer, S.: Wit-uas: A wildland-fire infrared thermal dataset to detect crew assets from aerial views. In: 2023 IEEE/RSJ International Conference on Intelligent Robots and Systems (IROS). pp. 11464–11471. IEEE (2023)
17. Lee, D.G., Jeon, M.H., Cho, Y., Kim, A.: Edge-guided multi-domain rgb-to-tir image translation for training vision tasks with challenging labels. In: 2023 IEEE International Conference on Robotics and Automation (ICRA). pp. 8291–8298. IEEE (2023)
18. Li, C., Xia, W., Yan, Y., Luo, B., Tang, J.: Segmenting objects in day and night: Edge-conditioned cnn for thermal image semantic segmentation. IEEE Transactions on Neural Networks and Learning Systems **32**(7), 3069–3082 (2020)
19. Liang, M., Hu, J., Bao, C., Feng, H., Deng, F., Lam, T.L.: Explicit attention-enhanced fusion for rgb-thermal perception tasks. IEEE Robotics and Automation Letters (2023)
20. Liu, J., Fan, X., Huang, Z., Wu, G., Liu, R., Zhong, W., Luo, Z.: Target-aware dual adversarial learning and a multi-scenario multi-modality benchmark to fuse infrared and visible for object detection. In: Proceedings of the IEEE/CVF Conference on Computer Vision and Pattern Recognition. pp. 5802–5811 (2022)
21. Liu, M.Y., Breuel, T., Kautz, J.: Unsupervised image-to-image translation networks. In: Conference on Neural Information Processing Systems (NeurIPS) (2017)
22. Liu, Z., Mao, H., Wu, C.Y., Feichtenhofer, C., Darrell, T., Xie, S.: A convnet for the 2020s. In: Proceedings of the IEEE/CVF conference on computer vision and pattern recognition. pp. 11976–11986 (2022)
23. Lyu, Y., Vosselman, G., Xia, G.S., Yilmaz, A., Yang, M.Y.: Uavid: A semantic segmentation dataset for uav imagery. ISPRS Journal of Photogrammetry and Remote Sensing **165**, 108 – 119 (2020). <https://doi.org/https://doi.org/10.1016/j.isprsjprs.2020.05.009>, <http://www.sciencedirect.com/science/article/pii/S0924271620301295>
24. Mehta, S., Rastegari, M.: Separable self-attention for mobile vision transformers. arXiv preprint arXiv:2206.02680 (2022)
25. Mostegel, C., Maurer, M., Heran, N., Pestana Puerta, J., Fraundorfer, F.: Semantic drone dataset (Jan 2019), <http://dronedataset.icg.tugraz.at/>, Last accessed on 2023-10-27
26. Nigam, I., Huang, C., Ramanan, D.: Ensemble knowledge transfer for semantic segmentation. In: 2018 IEEE Winter Conference on Applications of Computer Vision (WACV). pp. 1499–1508. IEEE (2018)
27. Nirgudkar, S., DeFilippo, M., Sacarny, M., Benjamin, M., Robinette, P.: Massmind: Massachusetts maritime infrared dataset. The International Journal of Robotics Research **42**(1-2), 21–32 (2023)
28. Oquab, M., Darcet, T., Moutakanni, T., Vo, H.V., Szafraniec, M., Khalidov, V., Fernandez, P., Haziza, D., Massa, F., El-Nouby, A., Howes, R., Huang, P.Y., Xu, H., Sharma, V., Li, S.W., Galuba, W., Rabbat, M., Assran, M., Ballas, N., Synnaeve, G., Misra, I., Jegou, H., Mairal, J., Labatut, P., Joulin, A., Bojanowski, P.: Dinov2: Learning robust visual features without supervision (2023)



29. Panetta, K., Shreyas Kamath, K.M., Rajeev, S., Agaian, S.S.: Ftnet: Feature transverse network for thermal image semantic segmentation. *IEEE Access* **9**, 145212–145227 (2021). <https://doi.org/10.1109/ACCESS.2021.3123066>
30. Paszke, A., Gross, S., Massa, F., Lerer, A., Bradbury, J., Chanan, G., Killeen, T., Lin, Z., Gimelshein, N., Antiga, L., et al.: Pytorch: An imperative style, high-performance deep learning library. *Advances in neural information processing systems* **32** (2019)
31. Poudel, R., Liwicki, S., Cipolla, R.: Fast-scnn: Fast semantic segmentation network. In: Sidorov, K., Hicks, Y. (eds.) *Proceedings of the British Machine Vision Conference (BMVC)*. pp. 187.1–187.12. BMVA Press (September 2019). <https://doi.org/10.5244/C.33.187>, <https://dx.doi.org/10.5244/C.33.187>
32. Qin, T., Li, P., Shen, S.: Vins-mono: A robust and versatile monocular visual-inertial state estimator. *IEEE Transactions on Robotics* **34**(4), 1004–1020 (2018)
33. Saharia, C., Chan, W., Chang, H., Lee, C., Ho, J., Salimans, T., Fleet, D., Norouzi, M.: Palette: Image-to-image diffusion models. In: *ACM SIGGRAPH 2022 Conference Proceedings*. pp. 1–10 (2022)
34. Shin, U., Lee, K., Kweon, I.S.: Complementary random masking for rgb-thermal semantic segmentation. In: *IEEE International Conference on Robotics and Automation* (2024)
35. Shin, U., Park, J., Kweon, I.S.: Deep depth estimation from thermal image. In: *Proceedings of the IEEE/CVF Conference on Computer Vision and Pattern Recognition*. pp. 1043–1053 (2023)
36. Shivakumar, S.S., Rodrigues, N., Zhou, A., Miller, I.D., Kumar, V., Taylor, C.J.: Pst900: Rgb-thermal calibration, dataset and segmentation network. In: *2020 IEEE international conference on robotics and automation (ICRA)*. pp. 9441–9447. *IEEE* (2020)
37. Speth, S., Goncalves, A., Rigault, B., Suzuki, S., Bouazizi, M., Matsuo, Y., Prendinger, H.: Deep learning with rgb and thermal images onboard a drone for monitoring operations. *Journal of Field Robotics* **39**(6), 840–868 (2022)
38. Suo, J., Wang, T., Zhang, X., Chen, H., Zhou, W., Shi, W.: Hit-uav: A high-altitude infrared thermal dataset for unmanned aerial vehicle-based object detection. *Scientific Data* **10**, 227 (2023)
39. Tan, M., Le, Q.: Efficientnet: Rethinking model scaling for convolutional neural networks. In: *International conference on machine learning*. pp. 6105–6114. *PMLR* (2019)
40. Vertens, J., Zürn, J., Burgard, W.: Heatnet: Bridging the day-night domain gap in semantic segmentation with thermal images. In: *2020 IEEE/RSJ International Conference on Intelligent Robots and Systems (IROS)*. pp. 8461–8468. *IEEE* (2020)
41. Wang, T.C., Liu, M.Y., Zhu, J.Y., Tao, A., Kautz, J., Catanzaro, B.: High-resolution image synthesis and semantic manipulation with conditional gans. In: *Proceedings of the IEEE Conference on Computer Vision and Pattern Recognition* (2018)
42. Xie, E., Wang, W., Yu, Z., Anandkumar, A., Alvarez, J.M., Luo, P.: Segformer: Simple and efficient design for semantic segmentation with transformers. In: *Neural Information Processing Systems (NeurIPS)* (2021)
43. Xie, S., Girshick, R., Dollár, P., Tu, Z., He, K.: Aggregated residual transformations for deep neural networks. In: *Proceedings of the IEEE conference on computer vision and pattern recognition*. pp. 1492–1500 (2017)
44. Xiong, H., Cai, W., Liu, Q.: Mcnet: Multi-level correction network for thermal image semantic segmentation of nighttime driving scene. *Infrared Physics & Technol-*

- ogy p. 103628 (2021). <https://doi.org/https://doi.org/10.1016/j.infrared.2020.103628>
45. Yun, S., Jung, M., Kim, J., Jung, S., Cho, Y., Jeon, M.H., Kim, G., Kim, A.: Sthereo: Stereo thermal dataset for research in odometry and mapping. In: 2022 IEEE/RSJ International Conference on Intelligent Robots and Systems (IROS). pp. 3857–3864. IEEE (2022)
  46. Zhang, J., Liu, R., Shi, H., Yang, K., Reiß, S., Peng, K., Fu, H., Wang, K., Stiefel-hagen, R.: Delivering arbitrary-modal semantic segmentation. In: CVPR (2023)
  47. Zhu, P., Wen, L., Du, D., Bian, X., Fan, H., Hu, Q., Ling, H.: Detection and tracking meet drones challenge. *IEEE Transactions on Pattern Analysis and Machine Intelligence* **44**(11), 7380–7399 (2021)